Vertical Nb/TiO$_x$/Nb Josephson Junctions Controlled by In-Plane Hot-Electron Injection

Zuyu Xu,[1] Shixian Chen,[1] Wanghao Tian,[1] Zaidong Qi,[1] Wencheng Yue,[1] Hongmei Du,[1]
Hancong Sun,[2] Caihong Zhang,[1] Jingbo Wu,[1] Sining Dong,[1] Yong-Lei Wang,[1] Weiwei Xu,[1]
Biaobing Jin,[1] Jian Chen,[1,2] Guozhu Sun,[1,2] Dieter Koelle,[3] Reinhold Kleiner,[3,*]
Huabing Wang,[1,2,†] and Peiheng Wu[1,2]

[1] *Research Institute of Superconductor Electronics, Nanjing University, Nanjing 210023, China*
[2] *Purple Mountain Laboratories, Nanjing 211111, China*
[3] *Physikalisches Institut and Center for Quantum Science in LISA$^+$, Universität Tübingen,
72076 Tübingen, Germany*

(Received 5 March 2020; revised 16 June 2020; accepted 23 June 2020; published 5 August 2020)

We fabricate vertical Nb/TiO$_x$/Nb Josephson junctions where the TiO$_x$ layer is mostly metallic but has a high-resistance interface with the top Nb electrode. Thus, the junctions are in essence of the superconductor–insulator–normal-metal–superconductor type. The TiO$_x$ layer extends beyond the junction area and allows one to send an in-plane current through the normal-metal layer of the junction. We investigate and analyze dc properties (critical current, current-voltage characteristics) as well as the behavior of the junctions in external microwave fields. We find a strong dependence of all properties on the voltage V_i applied across the TiO$_x$ lead. The dependence on V_i can be mapped to the dependence of the junction parameters on the bath temperature T, when V_i is converted to an effective electronic temperature via $T_e = [T^2 + (aV_i)^2]^{1/2}$, with $a = 3.14$ K/mV. This relation was used before in the context of a metallic nanowire contacted by superconducting electrodes. While the geometry of our TiO$_x$ layer is far from that of a nanowire, the scaling works perfectly well for all experimental data. Our data also indicate that the electronic temperature is homogeneous throughout the junction area, a result that is unexpected for the large junction sizes we use. The device allows easy and relatively fast *in situ* manipulation of the junction parameters.

DOI: 10.1103/PhysRevApplied.14.024008

I. INTRODUCTION

Titanium (Ti) and its oxides (TiO$_x$) have attracted significant interest due to their diverse physical properties. For example, pure Ti can be used to contact monolayer transition-metal-dichalcogenide semiconductors [1]. TiO$_x$ is metallic for $x \approx 1$ and can even be a superconductor [2–4]. For $x \approx 2$, TiO$_x$ is semiconducting [5], and higher oxidation stages such as Ti$_4$O$_7$ exhibit metal-insulator or semiconductor-insulator transitions [6,7].

This richness in physical properties caught our interest to use TiO$_x$ as an interfacial layer for Josephson junctions and study their properties. The structures we investigate are vertical Nb/TiO$_x$/Nb Josephson junctions. To produce the TiO$_x$ barrier, we deposit Ti on top of the bottom Nb electrode and subsequently oxidize it. As we will see, the oxidation stage of TiO$_x$ is mostly near $x = 1$—that is, the barrier layer is metallic—but there is also a high-resistance interface with the upper Nb electrode. TiO$_x$ with $x \approx 2$ may have formed here. In our layout we extend the TiO$_x$ layer outside the actual junction area to a long stripe and contact it, allowing us to send in-plane currents through the TiO$_x$ film. Over the years, tuning the electronic properties of Josephson junctions containing a normal-metal (N) barrier by hot electrons flowing along the N layer [8–38] has become an interesting alternative to gating [39–51].

While most of the studies mentioned above used mesoscopic planar structures, the geometry we investigate is similar to the one studied in Refs. [25,26,28,29], where a normal-Al layer was sandwiched between two insulating AlO$_x$ layers and contacted by Nb, forming a vertical superconductor–insulator–normal-metal–insulator–superconductor (S-I-N-I-S) structure, with tunnelinglike current-voltage characteristics (IVCs) and the possibility to send a current along the N layer. The other structure with which we want to compare our geometry is the planar superconductor–normal-metal–superconductor (S-N-S) junction investigated in Refs. [11,15,16], where a Au nanowire was contacted

---

[*] kleiner@uni-tuebingen.de
[†] hbwang@nju.edu.cn

by Nb. For this geometry, the authors showed that, as a result of hot-electron diffusion into the junction, the IVCs as well as the junction critical current I_c strongly varied when the nanowire was biased. The variations of the IVC and of I_c could be mapped to variations in the bath temperature T by assuming an effective electronic temperature $T_e = [T^2 + (aV_i)^2]^{1/2}$, where V_i is the voltage along the nanowire and $a = 6$ K/mV. Such a relation was suggested for mesoscopic nanowires [9,10] and was also used in Ref. [14] in the context of two-dimensional electron-gas–niobium structures, with $a = 3.2$ K/mV. Unfortunately, no corresponding information seems to be available for the *S-I-N-I-S* junction mentioned above.

Our junctions are in essence of the superconductor–insulator–normal-metal–superconductor (*S-I-N-S*) type, where for simplicity we call the high-resistance interface with Nb an “insulator,” and thus are in between the *S-I-N-I-S* and *S-N-S* junction types mentioned above. Although our *N* layer is several micrometers wide and far from being a nanowire, we find that all properties we see can be very well described by the same expression for T_e, although with a somewhat different value for a, which is 3.14 K/mV in our case. The scaling holds not only for the previously studied dc properties such as I_c and the IVC but also for the behavior of our junction in microwave fields, which we study in addition. The simple scaling provides easy understanding of our “macroscopic” vertical Nb/TiO$_x$/Nb Josephson junction and may lead to the possibility of experiments manipulating the electric parameters of this type of junction *in situ*.

II. SAMPLE FABRICATION

Figure 1(a) shows a scanning-electron-microscope (SEM) image of the Nb/TiO$_x$/Nb Josephson junctions. A SEM image on a larger scale is shown in the inset in Fig. 1(d). To create the device we first sputter a 120-nm-thick Nb film on a sapphire substrate. The bottom Nb electrode is patterned by a lift-off technique and by laser-writing photolithography. We then etch down the surface of the bottom Nb layer by about 5 nm by *in situ* Ar-ion milling to obtain a good contact to the 10-nm-thick Ti layer, which we sputter and pattern in the next step on top of the Nb layer. The length of the central rectangular part of the Ti stripe is 76 μm and its width is 28 μm. The outer parts have a width of 52 μm. We next oxidize the Ti layer in pure oxygen for 3 h at a pressure of 500 Pa. After oxidization, the 120-nm-thick top Nb film is deposited and patterned by laser-writing lithography and lift-off into the three top electrodes overlapping the TiO$_x$ layer and the bottom Nb electrode. The three junctions are labeled “JJ1” to “JJ3” and have lateral dimensions of 5 × 5 μm^2, 10 × 10 μm^2, and 15 × 15 μm^2, respectively. Below we discuss data regarding JJ2. Figure 1(b) shows a schematic cross section through one of the junctions together with the wiring scheme. The current flowing across the junction is I and the voltage across the junction is V. The current flowing along the TiO$_x$ layer is I_i and the voltage along the TiO$_x$ stripe is V_i. The TiO$_x$ layer is contacted from the top and from the bottom by Nb at a distance of about 28 μm from the central part, as can be seen from the inset in Fig. 1(d). A current source is used to bias this layer and the voltage V_i is recorded.

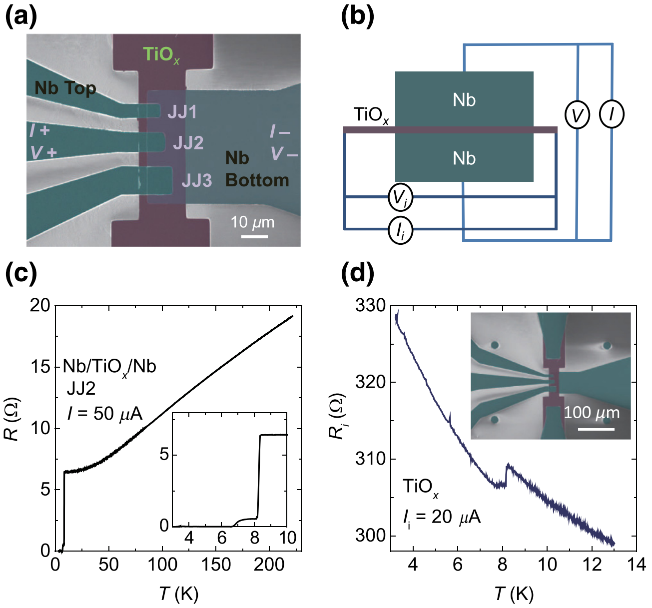

FIG. 1. Sample layout and characterization: (a) SEM image of the structure investigated. (b) Cross section through one of the junctions together with the wiring scheme. (c) Resistance R across JJ2 versus temperature. The inset shows the resistive transition of JJ2 on an enlarged scale. (d) Resistance R_i along the TiO$_x$ stripe versus temperature. The inset shows a SEM image of the structure on a larger scale than in (a).

Figure 1(c) displays the temperature dependence of the resistance $R = V/I$ measured across JJ2. The current I is set to 50 μA. The Nb film becomes superconducting at 8.3 K, while there is still a finite resistance due to the junction down to about 6.6 K. Zero resistance is reached when the junction critical current exceeds I. As we show below, the actual temperature where the critical current of JJ2 becomes nonzero is about 7.8 K. The resistance $R_i = V_i/I_i$ is shown in Fig. 1(d). The current I_i is set to 20 μA. R_i is about 300 Ω at 13 K and increases somewhat to about 330 Ω at 3.2 K. The geometry we use is not ideal to derive the resistivity from the data. Major parts of the central part of the TiO$_x$ are shunted by the bottom Nb electrode and make only a minor contribution to R_i at least when Nb is in the normal state. The same holds for the Nb electrodes contacting the TiO$_x$ stripe. Considering only the nonshunted areas between the ends of the Nb contacts and the bottom Nb electrode, one finds a resistivity of roughly 120–150 $\mu\Omega$ cm, which is clearly on the metallic side. The temperature dependence of R_i we observe and the magnitude of the specific resistance are typical for TiO [2]. The superconducting transition of Nb is also visible as a 1% jump in the R_i-versus-T curve. This is the contribution of the areas contacted by Nb. For $I_i = 20\ \mu$A, V_i exceeds 6 mV below T_c, and the electronic temperature T_e used to describe the properties of JJ2 exceeds 20 K (we find $a = 3.14$ K/mV). We thus assume that electrons flowing along the TiO$_x$ layer can freely penetrate at least the lower Nb electrode at all bath temperatures. Furthermore, as we see below, from the transport characteristics of JJ2 we find an out-of-plane resistance of about 0.56 Ω, which is more than a factor of 5000 larger than what we would expect from the resistivity of the TiO$_x$ layer measured in the plane. This indicates that we have a high-resistivity interface with the upper Nb electrode, caused either by higher oxidation stages of TiO$_x$, presumably with $x \approx 2$, or by some interface degradation during the lift-off patterning of the upper Nb electrode.

We next characterize JJ2 for $V_\mathrm{i} = 0$. Figures 2(a) and 2(b) show by purple and olive symbols the IVCs at a bath temperature of 2.8 K for current ranges near the junction critical current and on much-larger current and voltage scales, respectively. As seen from Fig. 2(a) the IVC is hysteretic, with critical current $I_c = 0.285$ mA (critical current density 285 A/cm^2) and return current $I_r = 0.167$ mA. Later, we compare the behavior of JJ2 with simulations performed with the resistively-and-capacitively-shunted-junction (RCSJ) model [52,53]. In this model the shape and hysteresis of the IVC are controlled by the Stewart-McCumber parameter $\beta_c = 2\pi I_c R^2 C/\Phi_0$, with C the junction capacitance and Φ_0 the flux quantum. We also include thermal noise, described by the noise parameter $\Gamma = 2\pi k_B T/I_c\Phi_0$, with k_B the Boltzmann constant. In the model the IVC approaches a *linear* junction resistance R for large currents and voltages. This cannot be reproduced here, because the IVC continues to be nonlinear for currents up to about 3 mA. We can still reproduce the hysteresis by using a linearized resistance $R_\mathrm{lin} = V_c/I_c = 1.1\ \Omega$, with $V_c = 0.32$ mV. As shown by the thin red line in Fig. 2(a), the hysteresis is described well for $\beta_c \approx 6$, yielding a capacitance of about 5.7 pF and a ratio ϵ/d_i of the dielectric constant ϵ to the "capacitor thickness" d_i of 6.4 nm^{-1}. The dielectric constant of TiO$_2$ can exceed 50, and thus a subnanometer-thick TiO$_2$ layer is sufficient to obtain this value [54]. In principle, the hysteresis in the IVC could also be of thermal origin [55,56]. However, the power density in our junction is very low, and in addition, as we see below, we can describe our microwave data very well with the RCSJ model. This would not be the case for a thermal origin of the hysteresis.

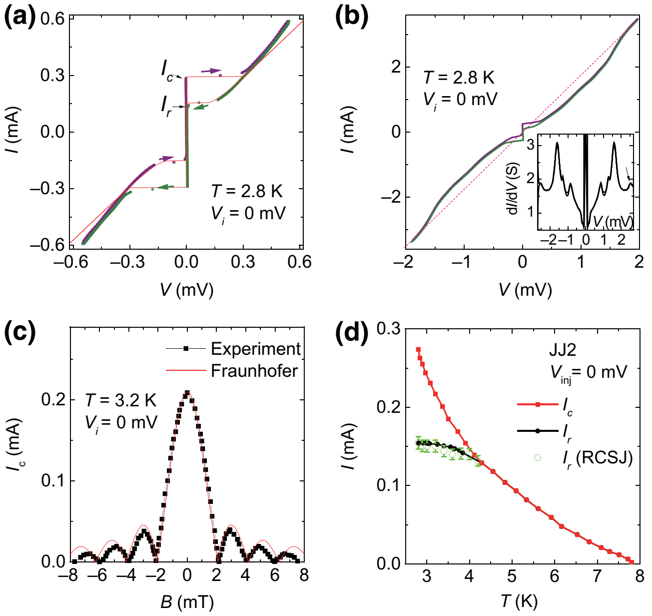

FIG. 2. Transport properties of JJ2 at $V_i = 0$. (a) IVC measured at $T = 2.8$ K with a current sweep from negative to positive (purple dots) and vice versa (olive dots). The thin red line is the IVC calculated from the RCSJ model using $\beta_c = 6$ and $\Gamma = 5 \times 10^{-4}$. (b) IVC at $T = 2.8$ K for voltages between -2 and 2 mV. The dotted line is a guide for the eye. The inset shows the differential conductance of JJ2. (c) Critical current versus magnetic field. The solid red line corresponds to the Fraunhofer pattern. (d) Temperature dependence of the critical current I_c and the return current I_r. The open symbols represent the return current, as calculated from the RCSJ model assuming a temperature-independent capacitance and using the measured values of the linearized resistance R_lin and the critical current I_c for each temperature. Error bars for the calculated return currents are indicated.

Figure 2(b) shows that the IVC continues to be nonlinear up to a voltage of about 1.9 mV, where the resistance reaches the aforementioned 0.56 Ω. We thus think that our junction is basically of the *S*-*I*-*N*-*S* type, and the nonlinear shape of the quasiparticle branch in the IVC below 1.9 mV reflects the fact that we are in the subgap regime. This picture is also supported by the differential-conductance-versus-V curve shown in the inset in Fig. 2(b). For a superconductor-insulator-superconductor (*S*-*I*-*S*) junction one would expect conductance peaks to occur at $2\Delta_\mathrm{Nb}/e$, where $2\Delta_\mathrm{Nb} \approx 2.7$ meV is twice the Nb energy gap. The conductance peak marked by the arrow in the inset is at 2.5 mV, which is close to that. The main peak occurs at 1.6 mV and there are additional peaks at 1.26 mV (about Δ_Nb/e) and at 0.83 mV (about $2\Delta_\mathrm{Nb}/3e$); the large peak at zero voltage is due to the Josephson current. Such a peak structure in the subgap regime can occur as a result of Andreev reflection and the formation of Andreev bound states, leading to a complicated density of states in the *N* region [57,58]. Furthermore, the maximum Joule-heat power in Fig. 2(b) is about 6 μW. The fact that we see a well-developed gap structure and the subgap peaks tells us that the maximum temperature rise by Joule heating must be much less than 5 K. This in turn implies that the possible temperature rise on the current and voltage scales of Fig. 2(a) is much less than 0.1 K.

Figure 2(c) shows the magnetic field dependence of the critical current, measured at 3.2 K. The field is oriented in the plane parallel to the TiO_x electrode [i.e., vertically in Fig. 1(a)]. Data are shown by the black symbols, and the red line corresponds to the Fraunhofer pattern for a perfectly homogeneous junction, $I_c(B) = I_c(0)\,|\sin x/x|$, with $x = \pi\Phi/\Phi_0$ and $\Phi = BWt_{\mathrm{eff}}$; $W = 10\ \mu$m is the width of the junction and $t_{\mathrm{eff}} \approx 2\lambda_L \tanh(d_{\mathrm{Nb}}/2\lambda_L) + d$ is the effective thickness of the junction [59], where d is the thickness of the TiO_x layer and λ_L is the London penetration depth. The experimental data are very close to the Fraunhofer pattern, showing good homogeneity of the Josephson critical current density. We further find $t_{\mathrm{eff}} = 100$ nm, which is close to what we would have expected for $\lambda_L \approx 80$ nm ($t_{\mathrm{eff}} \approx 110$ nm). Finally, Fig. 2(d) displays the temperature dependence of I_c and I_r. I_c is roughly linear for temperatures between 6 and 7.8 K and exhibits a negative curvature at temperatures down to 2.8 K, a behavior that is somewhere between the linear $I_c(T)$ dependence of *S*-*I*-*S* junctions near T_{c} and the parabolic $I_c(T)$ dependence of *S*-*N*-*S* junctions. Figure 2(d) also shows by the open symbols the return currents, as calculated from the RCSJ model assuming a temperature-independent capacitance and with the measured values of the linearized resistance R_{lin} and the critical current I_c for each temperature to calculate β_c for each temperature. The agreement with the measured values of I_r is fair, although there are large error bars arising from uncertainties in determining I_c and R_{lin}.

We mention here that the IVCs of JJ1 and JJ3—these junctions were only precharacterized so far—are similar to the IVC of JJ1 but not identical. At 2.8 K, JJ1 (JJ3) has a critical current density of 640 $\mathrm{A/cm^2}$ (490 $\mathrm{A/cm^2}$). The return current of JJ1 (JJ3) amounts to 88% (72%) of I_c, and V_c is 0.18 mV (0.25 mV). Thus, there is some variation over the chip which, however, seems to have a minor impact on the homogeneity of a given junction.

We next discuss the effect of nonzero V_i on the transport characteristics of JJ2. Like in Refs. [11,15], we describe the effect of electrons injected in the plane into the *N* layer by an effective electronic temperature $T_e = [T^2 + (aV_i)^2]^{0.5}$. We show below that this scaling works extremely well for our data. We find the parameter a to be 3.14 K/mV, which is very close to the theoretical value $a = 1/2L_0^{1/2} = 3.2$ K/mV, where L_0 is the Lorenz number [10,11]. However, for our complicated wiring scheme, the agreement is presumably accidental.

We first display in Fig. 3(a) IVCs of JJ2 for currents near the critical current for four values of V_i: 0, 1, 1.7, and 2.2 mV. Data are obtained at a bath temperature of 2.8 K. The IVCs strongly depend on V_i. Using the above value for a, we obtain effective temperatures of 2.8, 4.21, 6.03, and 7.46 K. Figure 3(b) displays IVCs obtained at similar bath temperatures at $V_i = 0$. The similarity to Fig. 3(a) is evident. We further convert V_i-dependent I_c and I_r data

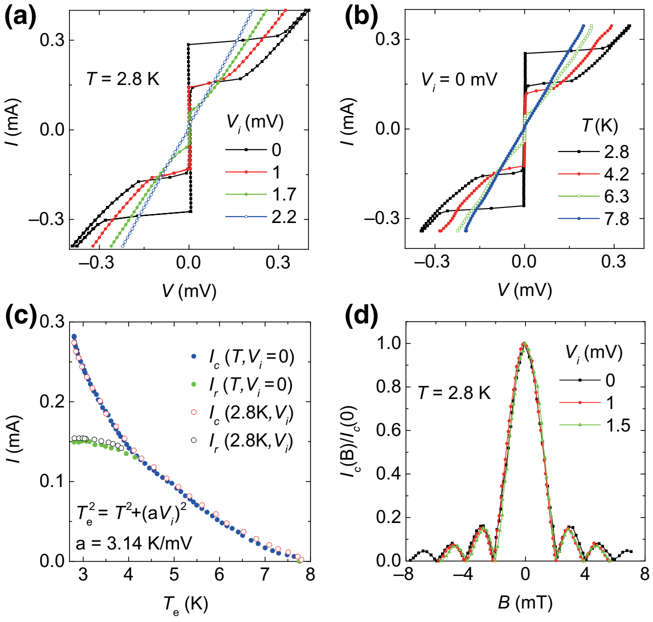

FIG. 3. Effect of nonzero values of V_i on transport properties of JJ2. (a) IVCs for four values of V_i at a bath temperature of 2.8 K. (b) IVCs for four values of T at $V_i = 0$. (c) I_c and I_r versus T_e, where $T_e^2 = T^2 + (aV_i)^2$, with $a = 3.14$ K/mV. The solid symbols are for variable T at $V_i = 0$ and the open symbols are for variable V_i at $T = 2.8$ K. (d) I_c versus B for three values of V_i at $T = 2.8$ K.

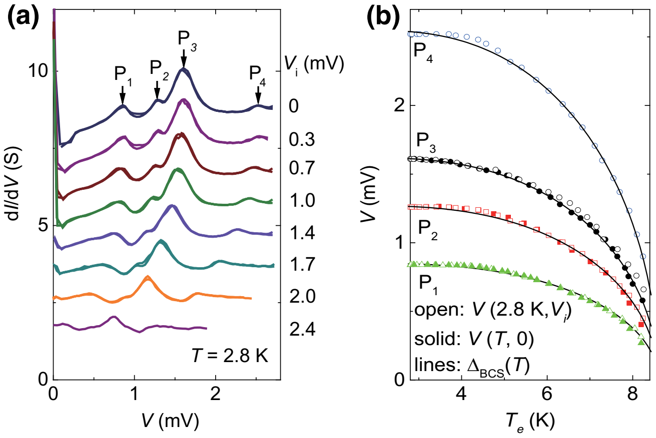

FIG. 4. Effect of nonzero values of V_i on transport properties of JJ2 at large voltage and current scales. (a) Differential conductance versus voltage for JJ2 at $T = 2.8$ K for eight different values of V_i. The main peaks are labeled "P_1" to "P_4." (b) Peak positions of P_1 to P_4 versus T_e for data obtained at $T = 2.8$ K and variable V_i (open symbols) and for $V_i = 0$ and variable T (solid symbols). The lines in (b) give the BCS temperature dependence of the energy gap.

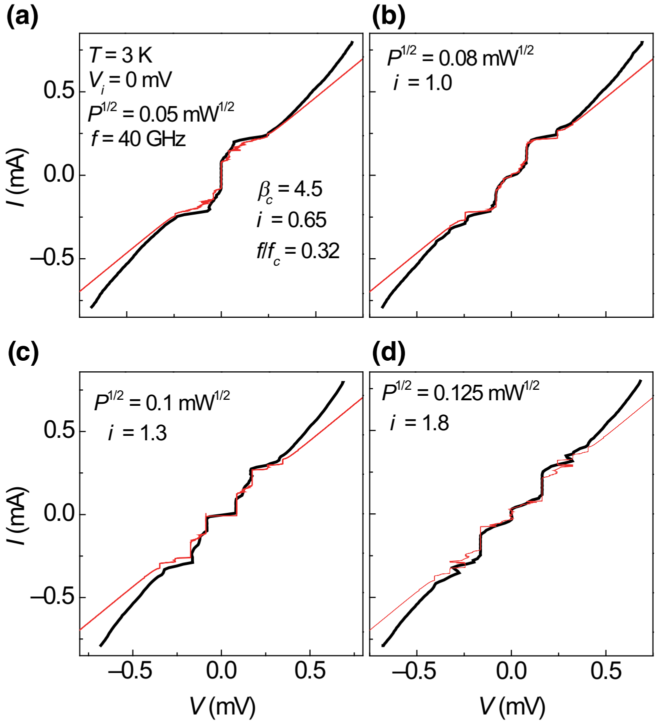

FIG. 5. Microwave properties: IVCs of JJ2 in a 40-GHz microwave field at $T = 3$ K and $V_i = 0$. Data, given by thick black lines, are for four different values of microwave power, with $P^{1/2} = 0.05$ mW$^{1/2}$ (a), $P^{1/2} = 0.08$ mW$^{1/2}$ (b), $P^{1/2} = 0.1$ mW$^{1/2}$ (c) and $P^{1/2} = 0.05$ mW$^{1/2}$ (d). Thin red lines are simulation results based on the RSCJ model, with $\beta_c = 4.5\, f_c = V_c/\Phi_0 = 125$ GHz, and $i = I_{\rm ac}/I_c = 0.65$ (a), $i = I_{\rm ac}/I_c = 1.0$ (b), $i = I_{\rm ac}/I_c = 1.3$ (c), and $i = I_{\rm ac}/I_c = 1.8$ (d).

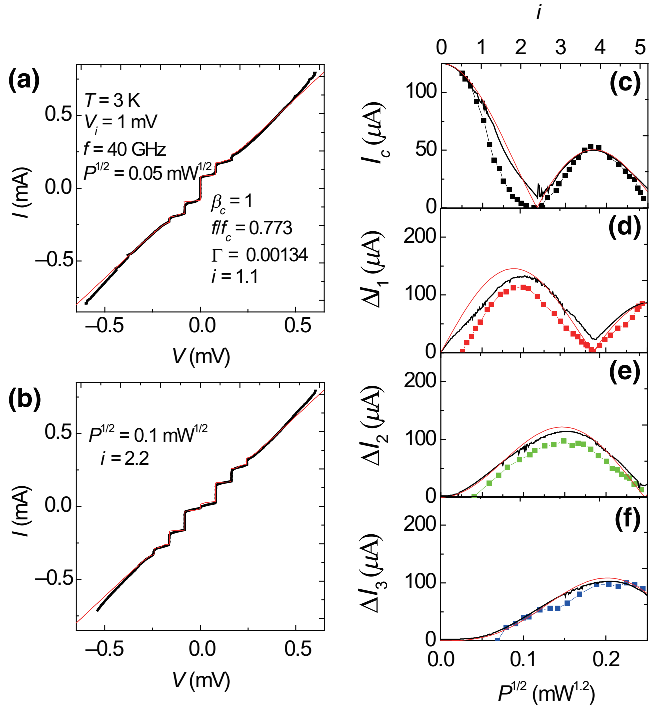

FIG. 6. Microwave properties: IVCs of JJ2 in a 40-GHz microwave field at $T = 3$ K and $V_i = 1$ mV for $P^{1/2} = 0.05$ mW$^{1/2}$ (a) and $P^{1/2} = 0.1$ mW$^{1/2}$ (b). Thin red lines are simulation results based on the RCSJ model, with parameters indicated in the graphs. In (c)–(f) the critical current (c) and the current-step height of the first (d), second, and third (f) Shapiro steps as a function of $P^{1/2}$ are indicated by symbols. The black lines are results from RCSJ simulations, and the red lines show Bessel functions J_0 to J_3 for comparison.

obtained at 2.8 K to T_e and compare them with I_c-versus-T and I_r-versus-T curves obtained at $V_i = 0$. The result is shown in Fig. 3(c). The agreement between the two data sets is excellent. Finally, we record I_c versus B for $V_i = 1$ and 1.5 mV and compare these data in normalized form with I_c versus B obtained at $V_i = 0$; see Fig. 3(d). All three curves basically are on top of each other, although that the zero-field critical current changes from 285 μA ($V_i = 0$) via 133 μA ($V_i = 1$ mV) to 76 μA ($V_i = 1.5$ mV). The perfect scaling of all three curves also implies that the electronic temperature in the Nb electrodes forming JJ2 does not vary in the direction perpendicular to the applied field.

The scaling also works in the high-bias regime. Figure 4(a) shows the differential conductance of JJ2 versus V recorded at $T = 2.8$ K for various values of V_i. For $V_i = 0$—this curve repeats the data shown in the inset in Fig. 2(b)—the main conductance peaks are labeled "P$_1$" to "P$_4$." As discussed above, P$_2$ is roughly located at $2\Delta_{\rm Nb}$. P$_3$ is located near $\Delta_{\rm Nb}$, whereas P$_1$ is close to $2\Delta_{\rm Nb}/3$, thus forming a series indicative of multiple Andreev-reflection processes. The four peaks shift to lower values of V with increasing V_i. In Fig. 4(b) we plot the voltage positions of peaks P$_1$ to P$_4$ as a function of T_e, where data are recorded either at $T = 2.8$ K and variable V_i (open symbols) or at $V_i = 0$ and variable T (solid symbols). Also these data scale excellently. In addition, we plot by solid lines the BCS temperature dependence of the Nb energy gap. The four peaks nicely follow these curves. Also this observation implies that T_e in both Nb electrodes has no gradients within the junction area. Otherwise we should see a broadening of the conductance peaks. This result comes as a surprise since, for the large junction sizes we use, one would at best expect that there are some nonequilibrium effects at the edges where the current is injected, healing out toward the center of the junction.

We now turn to the question of whether the injection effect can be used to control the microwave properties of our junction. While we are not equipped to vary V_i and thus T_e on fast timescales, we can study IVCs in external microwave fields. Figure 5 shows by thick black lines data obtained at 40 GHz, $T = 3$ K, and $V_i = 0$ for four values of microwave power P, referred to the the output of the microwave generator. Numbers are given as the microwave amplitude $P^{1/2}$. In all cases we observe only unstable Shapiro steps; that is, the junction is in a chaotic regime [60]. To analyze this more clearly, we perform simulations on the basis of the RCSJ model where the microwaves are modeled as alternating currents $I_{\mathrm{ac}} \propto P^{1/2}$ across the junction. We also include thermal noise in the simulations. The model parameters β_c and $f_c = V_c/\Phi_0$ are inferred from the IVC in the absence of microwaves, and thus there is no free parameter in the simulation. Also the simulated curves show the effect of chaos. When V_i is turned on, it is possible to tune the junction into a stable regime, as shown in Figs. 6(a) and 6(b) for two experimental IVCs (thick black lines) in comparison with the results of RCSJ simulations (thin red lines). The data are for 40 GHz, $T = 3$ K, and $V_i = 1$ mV. The parameters for the RCSJ simulations are indicated in the graphs and are extracted from a comparison with the experimental IVCs in the absence of microwaves. The stability of the Shapiro steps allows us to plot the critical current as well as the current-step height of the Shapiro steps as a function of microwave amplitude $P^{1/2}$. This is shown in Fig. 6(c) for I_c and in Figs. 6(d)–6(f) for the first, second, and third Shapiro steps. Experimental data are shown by symbols and the results of the RCSJ simulations are shown by thick black lines. For comparison, we also include the Bessel functions J_0 to J_3, describing the dependence of the critical current and the heights of the first, second, and third Shapiro steps, respectively, as a function of microwave amplitude in a voltage-biased situation that can also be obtained in the RCSJ simulations in some limiting cases; for example, when the microwave frequency approaches or exceeds f_c (in our case $f/f_c = 0.773$). As can be seen, the overall agreement is very good, and we show this in more detail in Fig. 7. In the graphs, the color scale is given by the differential resistance of the junction, plotted as a function of microwave amplitude and current I. Figures 7(a) and 7(c) show experimental data and Figs. 7(b) and 7(d) show the corresponding simulation results. The black parts in essence give the current regions where the differential resistance is zero (i e., where the junction is either in the zero-voltage state or in a region where a Shapiro step has formed). Figure 7(a) shows the case of $f = 40$ GHz and $V_i = 0$ (cf. Fig. 5) and Fig. 7(b) shows the corresponding simulation. Although the junction dynamics is chaotic, there is excellent agreement between experiment and simulation. Figure 7(c) show the case of $f = 40$ GHz and $V_i = 1$ mV (cf. Fig. 6) and Fig. 7(d) shows the corresponding simulation. Also here the agreement is very good, showing in total that JJ2 is well behaved and controllable also in microwave fields.

For completeness, Fig. 8 demonstrates this for a different microwave frequency, 25 GHz. The graphs are organized like Fig. 7, and we use the same values of the McCumber parameter and the characteristic frequency as for the 40-GHz data. At $V_i = 0$ [see Fig. 8(a)] the junction is again close to a chaotic regime, while for $V_i = 1$ mV it is basically stable. Like for the 40-GHz data the agreement between experiment and simulation is excellent.

We finally comment on the presumed speed of changing T_e. For the nanostructure described in Ref. [11], the relevant timescale is the electron diffusion time $\tau_D = L^2/D \sim 20$ ps, where $L \sim 0.7$ μm is the length of the nanowire and D is the electronic diffusion constant of Au. In our

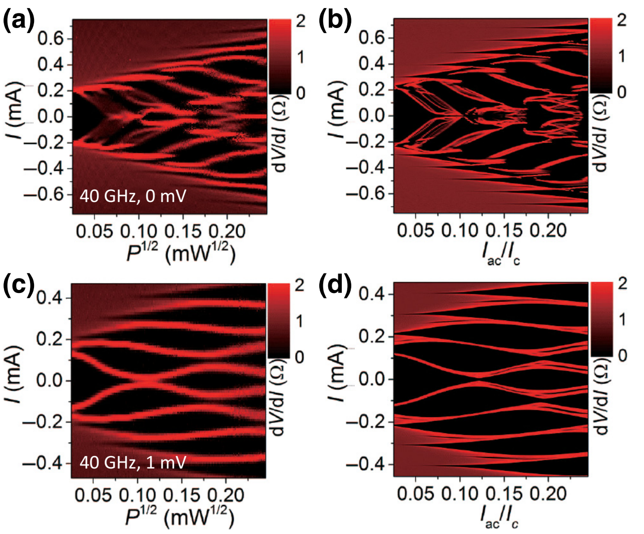

FIG. 7. Microwave properties: color plot of the junction differential resistance versus microwave amplitude and bias current I for a 40-GHz microwave field at $T = 3$ K. (a),(c) Experimental data for $V_i = 0$ (a) and $V_i = 1$ mV (c). (b),(d) The results of corresponding RCSJ simulations.

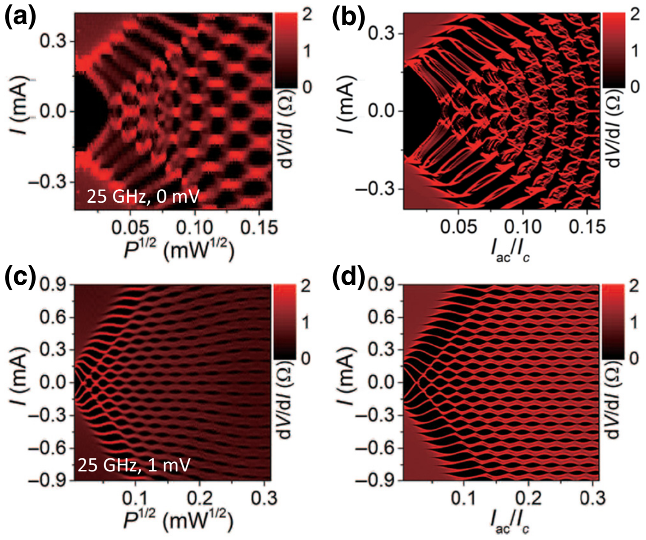

FIG. 8. Microwave properties: color plot of the junction differential resistance versus microwave amplitude and bias current I for a 25-GHz microwave field at $T = 3$ K. (a),(c) Experimental data for $V_i = 0$ (a) and $V_i = 1$ mV (c). (b),(d) The results of corresponding RCSJ simulations.

case, we should replace L by the 68-μm width of the lower electrode. We do not know the diffusion time of TiO but we do not think it will be shorter than that of Au. Consequently, we expect τ_D to be on the scale of some hundred nanoseconds. Narrowing the lower Nb electrode might reduce this number by a factor of 50 or so, but still we would expect the maximum operation frequencies of our device to be restricted to the subgigahertz range. Thus, the device can be modulated quickly, but not ultraquickly.

III. CONCLUSIONS

In summary, we fabricate a multiterminal vertical Nb/TiO$_x$/Nb Josephson junction allowing us to send an in-plane current along the TiO$_x$ layer. Our structure in essence forms a *S*-*I*-*N*-*S* Josephson junction with the possibility to alter all junction parameters via the in-plane flow of hot electrons. We use the electronic temperature $T_e = [T^2 + (aV_i)^2]^{1/2}$, where T is the bath temperature, V_i is the voltage along the TiO$_x$ layer, and $a = 3.14$ K/mV, to relate the changes in electric properties induced by the hot-electron flow to the changes induced by our varying the bath temperature. The relation was previously used in the context of planar *S*-*N*-*S* junctions where Nb electrodes contacted a Au nanowire [11,15,16]. While the geometry of our TiO$_x$ layer is far from that of a nanowire, the scaling works perfectly for all the measurements we make, including the appearance of Shapiro steps in external microwave fields. This may allow, for example, fast and controlled modulation of the junction parameters. This may be stabler and is definitely faster than changing the bath temperature. Our data show that a spatially homogeneous electronic temperature can be obtained even on a 100-μm scale, and thus a large variety of junction sizes from the nanoscale to the macroscopic level can be investigated. For example, a study of nonequilibrium physics in general will be interesting. On the more applied side, one could think of parametric amplification or of transistorlike configurations, although it presently seems that the maximum operation frequencies are in the subgigahertz range.

ACKNOWLEDGMENTS

We gratefully acknowledge financial support by the National Natural Science Foundation of China (Grants No. 61727805, No. 11961141002, No. 61521001, and No. 61771235), the National Key R&D Program of China (Grants No. 2018YFA0209002 and No. 2016YFA0301802), Jiangsu Key Laboratory of Advanced Techniques for Manipulating Electromagnetic Waves, the Priority Academic Program Development of Jiangsu Higher Education Institutions (PAPD), RFBR Grant No. 17-52-12051, European Union Sixth Framework Programme COST Action CA16218, and the Deutsche Forschungsgemeinschaft via project KL930-13/2.

[1] J. H. Kang, W. Liu, D. Sarkar, D. Jena, and K. Banerjee, Computational Study of Metal Contacts to Monolayer Transition-Metal Dichalcogenide Semiconductors, Phys. Rev. X **4**, 031005 (2014).

[2] P. Denker, Electronic properties of titanium monoxide, J. Appl. Phys. **37**, 142 (1966).

[3] J. K. Hulm, C. K. Jones, R. A. Hein, and J. W. Gibson, Superconductivity in the TiO and NbO systems, J. Low Temp. Phys. **7**, 291 (1972).

[4] C. Zhang, F. Hao, G. Gao, X. Liu, C. Ma, Y. Lin, Y. Yin, and X. Li, Enhanced superconductivity in TiO epitaxial thin films, npj Quant. Mater. **2**, 2 (2017).

[5] R. G. Breckenridge and W. R. Hosler, Electrical properties of titanium dioxide semiconductors, Phys. Rev. **91**, 793 (1953).

[6] R. F. Bartholomew and D. R. Frankl, Electrical properties of some titanium oxides, Phys. Rev. **187**, 828 (1969).

[7] C. Schlenker, S. Lakkis, J. M. D. Coey, and M. Marezio, Heat Capacity and Metal-Insulator Transitions in Ti$_4$O$_7$ Single Crystals, Phys. Rev. Lett. **32**, 1318 (1974).

[8] T. Wong, J. T. C. Yeh, and D. N. Langenberg, Quasiparticle-Injection-Induced Superconducting Weak Links, Phys. Rev. Lett. **37**, 150 (1976).

[9] H. Pothier, S. Guéron, Norman O. Birge, D. Esteve, and M. H. Devoret, Energy Distribution Function of Quasiparticles in Mesoscopic Wires, Phys. Rev. Lett. **79**, 3490 (1997).

[10] H. Pothier, S. Guéron, Norman O. Birge, D. Esteve, and M. H. Devoret, Energy distribution of electrons in an out-of-equilibrium metallic wire, Z. Phys. B **104**, 178 (1997).

[11] A. F. Morpurgo, T. M. Klapwijk, and B. J. van Wees, Hot electron tunable supercurrent, Appl. Phys. Lett. **72**, 966 (1998).

[12] F. K. Wilhelm, G. Schön, and A. D. Zaikin, Mesoscopic Superconducting–Normal Metal–Superconducting Transistor, Phys. Rev. Lett. **81**, 1682 (1998).

[13] Th. Schäpers, J. Malindretos, K. Neurohr, S. Lachenmann, A. van der Hart, G. Crecelius, H. Hardtdegen, and H. Lüth, Demonstration of a current-controlled three-terminal Nb–In$_x$Ga$_{1-x}$As/InP Josephson contact, Appl. Phys. Lett. **73**, 2348 (1998).

[14] K. Neurohr, Th. Schäpers, J. Malindretos, S. Lachenmann, A. I. Braginski, H. Lüth, M. Behet, G. Borghs, and A. A. Golubov, Local suppression of Josephson currents in niobium/two-dimensional electron gas/niobium structures by an injection current, Phys. Rev. B **59**, 11197 (1999).

[15] J. J. A. Baselmans, A. F. Morpurgo, B. J. van Wees, and T. M. Klapwijk, Tunable supercurrent in superconductor/normal metal/superconductor Josephson junctions, Superlattices Microstruct. **25**, 973 (1999).

[16] J. J. A. Baselmans, A. F. Morpurgo, B. J. van Wees, and T. M. Klapwijk, Reversing the direction of the supercurrent in a controllable Josephson junction, Nature **397**, 43 (1999).

[17] J. Kutchinsky, R. Taboryski, C. B. Sørensen, J. B. Hansen, and P. E. Lindelof, Observation of Supercurrent Enhancement in SNS Junctions by Nonequilibrium Injection into Supercurrent Carrying Bound Andreev States, Phys. Rev. Lett. **83**, 4856 (1999).

[18] P. Samuelsson, J. Lantz, V. S. Shumeiko, and G. Wendin, Nonequilibrium Josephson effect in mesoscopic ballistic multiterminal SNS junctions, Phys. Rev. B **62**, 1319 (2000).

[19] R. Shaikhaidarov, A. F. Volkov, H. Takayanagi, V. T. Petrashov, and P. Delsing, Josephson effects in a superconductor–normal-metal mesoscopic structure with a dangling superconducting arm, Phys. Rev. B **62**, R14649 (2000).

[20] J. J. A. Baselmans, B. J. van Wees, and T. M. Klapwijk, Nonequilibrium supercurrent transport in controllable superconductor–normal-metal–superconductor junctions, Phys. Rev. B **63**, 094504 (2001).

[21] J. Huang, F. Pierre, T. T. Heikkilä, F. K. Wilhelm, and N. O. Birge, Observation of a controllable π junction in a 3-terminal Josephson device, Phys. Rev. B **66**, 020507 (2002).

[22] Th. Schäpers, V. A. Guzenko, R. P. Müller, A. A. Golubov, A. Brinkman, G. Crecelius, A. Kaluza, and H. Lüth, Current-injection in a ballistic multiterminal superconductor/two-dimensional electron gas Josephson junction, Phys. Rev. B **67**, 014522 (2003).

[23] A. M. Savin, J. P. Pekola, J. T. Flyktman, A. Anthore, and F. Giazotto, Cold electron Josephson transistor, Appl. Phys. Lett. **84**, 4179 (2004).

[24] M. S. Crosser, P. Virtanen, T. T. Heikkilä, and N. O. Birge, Supercurrent-Induced Temperature Gradient across a Nonequilibrium SNS Josephson Junction, Phys. Rev. Lett. **96**, 167004 (2006).

[25] I. P. Nevirkovets, O. Chernyashevskyy, and J. B. Ketterson, Direct Study of the Proximity Effect in the Normal Layer inside of the Stacked SINIS Device, Phys. Rev. Lett. **95**, 247008 (2005).

[26] I. P. Nevirkovets, O. Chernyashevskyy, J. B. Ketterson, and E. Goldobin, Fabrication and characterization of multiterminal superconductor-insulator-normal metal-insulator-superconductor Josephson devices, J. Appl. Phys. **97**, 123903 (2005).

[27] I. P. Nevirkovets, O. Chernyashevskyy, and J. B. Ketterson, Absence of enhanced superconductivity in double-barrier superconducting tunnel junctions: Measurements of lateral electric transport in the middle normal-metal layer, Phys. Rev. B **73**, 224521 (2006).

[28] I. P. Nevirkovets, S. E. Shafranjuk, O. Chernyashevskyy, and J. B. Ketterson, Enhancement of the Josephson critical current in a multiterminal SINIS device under current injection, Phys. Rev. B **76**, 184520 (2007).

[29] I. P. Nevirkovets, S. E. Shafranjuk, O. Chernyashevskyy, and J. B. Ketterson, Enhancement of the Supercurrent at a Finite Voltage in a Sandwich-Type Ballistic SINIS Junction, Phys. Rev. Lett. **98**, 127002 (2007).

[30] O.-P. Saira, M. Meschke, F. Giazotto, A. M. Savin, M. Möttönen, and J. P. Pekola, Heat Transistor: Demonstration of Gate-Controlled Electronic Refrigeration, Phys. Rev. Lett. **99**, 027203 (2007).

[31] M. S. Crosser, J. Huang, F. Pierre, P. Virtanen, T. T. Heikkilä, F. K. Wilhelm, and N. O. Birge, Nonequilibrium transport in mesoscopic multi-terminal SNS Josephson junctions, Phys. Rev. B **77**, 014528 (2008).

[32] S. Tirelli, A. M. Savin, C. Pascual Garcia, J. P. Pekola, F. Beltram, and F. Giazotto, Manipulation and Generation of Supercurrent in Out-of-Equilibrium Josephson Tunnel Nanojunctions, Phys. Rev. Lett. **101**, 077004 (2008).

[33] I. A. Devyatov and M. Yu. Kupriyanov, High sensitivity microwave detector based on a Josephson heterostructure, JETP Lett. **89**, 451 (2009).

[34] F. Giazotto, J. T. Peltonen, M. Meschke, and J. P. Pekola, Superconducting quantum interference proximity transistor, Nat. Phys. **6**, 254 (2010).

[35] S. Roddaro, A. Pescaglini, D. Ercolani, L Sorba, F. Giazotto, and F. Beltram, Hot-electron effects in InAs nanowire Josephson junctions, Nano Res. **11**, 259 (2011).

[36] S. Mai, E. Kandelaki, A. Volkov, and K. Efetov, Stationary Josephson effect in a short multiterminal junction, Phys. Rev. B **87**, 024507 (2013).

[37] A. W. Draelos, M.-T. Wei, A. Seredinski, H. Li, Y. Mehta, K. Watanabe, T. Taniguchi, I. V. Borzenets, F. Amet, and G. Finkelstein, Supercurrent flow in multiterminal graphene Josephson junctions, Nano Lett. **19**, 1039 (2019).

[38] M. P. Nowak, M. Wimmer, and A. R. Akhmerov, Supercurrent carried by nonequilibrium quasiparticles in a multiterminal Josephson junction, Phys. Rev. B **99**, 075416 (2019).

[39] A. Chrestin, T. Matsuyama, and U. Merkt, Critical currents and supercurrent oscillations in Josephson field-effect transistors, Phys. Rev. B **49**, 498 (1994).

[40] M. R. Buitelaar, T. Nussbaumer, and C. Schönenberger, Quantum Dot in the Kondo Regime Coupled to Superconductors, Phys. Rev. Lett. **89**, 256801 (2002).

[41] P. Jarillo-Herrero, J. A. van Dam, and L. P. Kouwenhoven, Quantum supercurrent transistors in carbon nanotubes, Nature **439**, 953 (2006).

[42] H. I. Jørgensen, K. Grove-Rasmussen, T. Novotný, K. Flensberg, and P. E. Lindelof, Electron Transport in Single-Wall Carbon Nanotube Weak Links in the Fabry-Perot Regime, Phys. Rev. Lett. **96**, 207003 (2006).

[43] J.-P. Cleuziou, W. Wernsdorfer, V. Bouchiat, T. Ondarcuhu, and M. Monthioux, Carbon nanotube superconducting quantum interference device, Nat. Nanotechnol. **1**, 53 (2006).

[44] J.-P. Cleuziou, W. Wernsdorfer, S. Andergassen, S. Florens, V. Bouchiat, Th. Ondarçuhu, and M. Monthioux, Gate-Tuned High Frequency Response of Carbon Nanotube Josephson Junctions, Phys. Rev. Lett. **99**, 117001 (2007).

[45] H. B. Heersche, P. Jarillo-Herrero, J. B. Oostinga, L. M. K. Vandersypen, and A. F. Morpurgo, Bipolar supercurrent in graphene, Nature **446**, 57 (2007).

[46] A. M. R. V. L. Monteiro, D. J. Groenendijk, N. Manca, E. Mulazimoglu, S. Goswami, Ya. Blanter, L. M. K. Vandersypen, and A. D. Caviglia, Side gate tunable Josephson junctions at the $\mathrm{LaAlO_3/SrTiO_3}$ interface, Nano Lett. **17**, 715 (2017).

[47] G. Nanda, J. L. Aguilera, P. Rakyta, A. Kormanyos, R. Kleiner, D. Koelle, K. Watanabe, T. Taniguchi, L. M. K. Vandersypen, and S. Goswami, Current-phase relation of ballistic graphene Josephson junctions, Nano Lett. **17**, 3396 (2017).

[48] Y. Cao, V. Fatemi, S. Fang, K. Watanabe, T. Taniguchi, E. Kaxiras, and P. Jarillo-Herrero, Unconventional superconductivity in magic-angle graphene superlattices, Nature **556**, 43 (2018).

[49] S. Hart, Z. Cui, G. Ménard, M. Deng, A. E. Antipov, R. M. Lutchyn, P. Krogstrup, C. M. Marcus, and K. A. Moler, Current-phase relations of InAs nanowire Josephson junctions: From interacting to multimode regimes, Phys. Rev. B **100**, 064523 (2019).

[50] F. Paolucci, F. Vischi, G. De Simoni, C. Guarcello, P. Solinas, and F. Giazotto, Field-effect controllable metallic Josephson interferometer, Nano Lett. **19**, 6263 (2019).

[51] J.-H. Choi, G.-H. Lee, S. Park, D. Jeong, J.-O. Lee, H.-S. Sim, Y.-J. Doh, and H.-J. Lee, Complete gate control of supercurrent in graphene p-n junctions, Nat. Commun. **4**, 2525 (2019).

[52] W. C. Stewart, Current-voltage characteristics of Josephson junctions, Appl. Phys. Lett. **12**, 277 (1968).

[53] D. E. McCumber, Effect of ac impedance on dc voltage-current characteristics of superconductor weak link junctions, J. Appl. Phys. **39**, 3113 (1968).

[54] G. P. Burns, Titanium dioxide dielectric films formed by rapid thermal oxidation, J. Appl. Phys. **65**, 2095 (1988).

[55] V. N. Gubankov, K. K. Likharev, and N. M. Margolin, Properties of superconducting point contacts, Sov. J. Fiz. Tverd.Tela **14**, 953 (1972).

[56] H. Courtois, M. Meschke, J. T. Peltonen, and J. P. Pekola, Origin of Hysteresis in a Proximity Josephson Junction, Phys. Rev. Lett. **101**, 067002 (2008).

[57] A. Brinkman, A. A. Golubov, H. Rogalla, F. K. Wilhelm, and M. Yu. Kupriyanov, Microscopic nonequilibrium theory of double-barrier Josephson junctions, Phys. Rev. B **68**, 224513 (2003).

[58] S. E. Shafranjuk and J. B. Ketterson, Resonant states of a double-barrier junction, Phys. Rev. B **72**, 024509 (2005).

[59] M. Weihnacht, Influence of film thickness on d. c. Josephson current, Phys. Stat. Sol. **32**, K169 (1969).

[60] R. L. Kautz and R. Monaco, Survey of chaos in the rf-biased Josephson junction, J. Appl. Phys. **57**, 875 (1984).